PAPER • OPEN ACCESS

A holographic GRIN lens for broadband, highly directive, and aberration-free echo detection

To cite this article: Jinhu Zhang *et al* 2026 *Int. J. Extrem. Manuf.* **8** 055505

OPEN ACCESS
IMMT | IOP Publishing

International Journal of Extreme Manufacturing

Int. J. Extrem. Manuf. 8 (2026) 055505 (15pp)

https://doi.org/10.1088/2631-7990/ae6b25

A holographic GRIN lens for broadband, highly directive, and aberration-free echo detection

Jinhu Zhang[1,§], Sheng Liu[1,§], Chen Yang[1], Nana Zhou[1], Erqian Dong[2], Zhenxuan Bu[1], Wei Zheng[1], Fei Zhang[1], Zhongchang Song[1] and Yu Zhang[1,3,*]

[1] Key Laboratory of Underwater Acoustic Communication and Marine Information Technology of the Ministry of Education, College of Ocean and Earth Sciences, Xiamen University, Xiamen 361005, People's Republic of China
[2] Department of Mechanical Engineering, University of Hong Kong, Hong Kong Special Administrative Region of China, People's Republic of China
[3] State Key Laboratory of Submarine Geoscience, School of Ocean and Civil Engineering, Shanghai Jiao Tong University, Shanghai 200240, People's Republic of China

E-mail: yuzhang2025@sjtu.edu.cn

Received 3 October 2025, revised 5 January 2026
Accepted for publication 9 May 2026
Published 8 June 2026

Abstract

Directing wave energy through strongly aberrating media poses a fundamental challenge in wave physics. This problem is especially critical in underwater acoustics, where the hydrodynamic domes of autonomous underwater vehicles inevitably distort sonar wavefronts. This aberration leads to degraded beam quality and a significantly reduced detection range. Here, we address this long-standing challenge with a passive and broadband holographic gradient-index lens designed based on time-reversal invariance and high-frequency approximation principles. The lens is realized with a soft, water-impedance-matched tungsten-silicone metamaterial with a highly stable refractive index under key marine environmental factors such as temperature and salinity. This allows the lens to powerfully correct severe aberrations while simultaneously collimating sound into a highly directive beam over a wide operational band of 20–45 kHz. This metamaterial-based approach achieves significant performance improvements, achieving approximately four-fold beam sharpening from over 65° to 16°–30° and increasing the on-axis source level by more than 10 dB. In practical underwater detection scenarios, it achieves over 10 dB of reverberation suppression and significantly increases the effective detection range. Our work establishes a new and versatile design platform for advanced wavefront engineering with broad application prospects in underwater acoustic sensing and beyond.

[§] These authors contributed equally to this work and should be considered co-first author.
[*] Author to whom any correspondence should be addressed.

Supplementary material for this article is available online

Keywords: aberration correction, holographic lens, soft metamaterial, broadband, AUV sonar

1. Introduction

Directing wave energy through strongly aberrating layers is a fundamental challenge in wave physics and is of great significance for the advancement of imaging, communications, and sensing. Even with a perfect hardware system, imaging quality can still be compromised because of inhomogeneities in the propagation medium. Spatial variations in wave velocity on large scales introduce aberrations when the wave passes through the medium. Irregularly distributed scatterers can also induce multiple scattering, further distorting the wavefront and causing waves to propagate in unpredictable directions. In underwater applications, autonomous underwater vehicles (AUVs) are indispensable tools for exploring the ocean, which covers over 70% of the Earth's surface but remains largely unexplored[1]. These platforms rely on sonar systems for navigation, communication, and environmental perception (Figure 1(a)). However, the long-standing paradox inherent in AUV design severely limits their acoustic performance. Hydrodynamic domes that protect sensitive sonar transducers and reduce drag introduce a complex, structurally non-uniform acoustic aberration layer[2–4]. As sound waves traverse these curved, multi-material layers, severe wavefront distortion occurs (Figure 1(b)). This aberration causes sound energy to scatter in unpredictable ways, producing high sidelobes, weakening the main beam, and significantly reducing the effective source level, which ultimately leads to a decrease in the detection range and resolution of the sonar.

Conventional approaches face challenges in addressing this issue. Active phased-array systems enable electronic scanning and dynamic beamforming. However, their inherent discretized and wavelength-comparable element structure, spaced at or near the Nyquist limit, fundamentally constrains the resolution and space-bandwidth product[5,6]. Furthermore, these active systems rely on complex, power-hungry electronic equipment, presenting severe size, weight, power, and cost (SWaP-C) challenges for compact, long-endurance AUVs. Alternatively, signal post-processing techniques can correct for known or estimated aberrations at the receiver using advanced algorithms[7–10]. Although these algorithms can partially improve image quality, they inherently cannot recover the acoustic energy lost due to scattering during transmission and reception. They also impose a significant computational burden that may hinder real-time operations. Therefore, a physical solution capable of passively correcting broadband aberrations at the source remains challenging.

Acoustic metamaterials, which are engineered composite materials with properties that cannot be achieved in nature, have opened up new paradigms for wave control, enabling functions such as subwavelength imaging, acoustic cloaking, beamforming, and so on[11–18]. Recently, in the fields of underwater acoustic communication and detection, metasurfaces have been proven to enhance sound transmission across water−air interfaces via impedance-matching structures[19–21], enable dynamic beam scanning for static passive meta-sonar[22], and realize sonar focusing imaging through phase encoding mechanisms[23]. In parallel, emerging holographic metasurfaces achieve precise localized acoustic scattering behavior by patterning subwavelength pixels at interfaces[24–31]. When realized through high-resolution manufacturing techniques such as 3D printing and paper cutting, this approach eliminates discretization effects and provides high space-bandwidth products. By synthesizing the required complex wavefronts, acoustic holography can compensate for severe distortions, enabling applications such as focusing acoustic vortices or generating arbitrary ultrasound fields through the human skull[32–34]. Complementary acoustic metamaterials have also shown potential in addressing aberration layers[35–37]. However, a fundamental challenge hinders the practical application of these technologies: the inherent dispersion characteristics of their resonant or diffractive elements limit their operational range to narrow bandwidths. This characteristic makes them incompatible with the broadband signals required by modern sonar systems. While tunable metasurfaces are being explored to overcome this, their complexity and insufficient refresh rates of current control technologies limit their application for real-time systems[38–40].

Here, we theoretically introduce and experimentally demonstrate a passive, broadband soft acoustic holographic gradient-index (GRIN) lens that corrects the severe aberrations caused by the AUV's dome. Our approach establishes a versatile design theory, based on time-reversal invariance and high-frequency approximations, for calculating the specific gradient-index profile required to compensate for the aberrations of any given dome (Figure 1(c)). We realized the required acoustic properties by synthesizing a soft, water-impedance-matched metamaterial from a silicone elastomer embedded with tungsten micro-particles. This soft metamaterial's refractive index remains highly stable against variations in key marine environmental factors such as temperature and salinity. Both simulations and underwater experiments show that our holographic GRIN lens can simultaneously eliminate phase aberrations from the dome and transform the weakly directional radiation from a compact sound source into a highly directional acoustic beam. This is quantified by a sharpening of the −3 dB beamwidth from exceeding 65° to below 30° and an on-axis source level enhancement of more than 10 dB. In typical underwater detection scenarios, our lens-enhanced echo detection system, fully compatible with modern broadband sonar signals, achieves significant performance improvements. The combination of higher directionality and

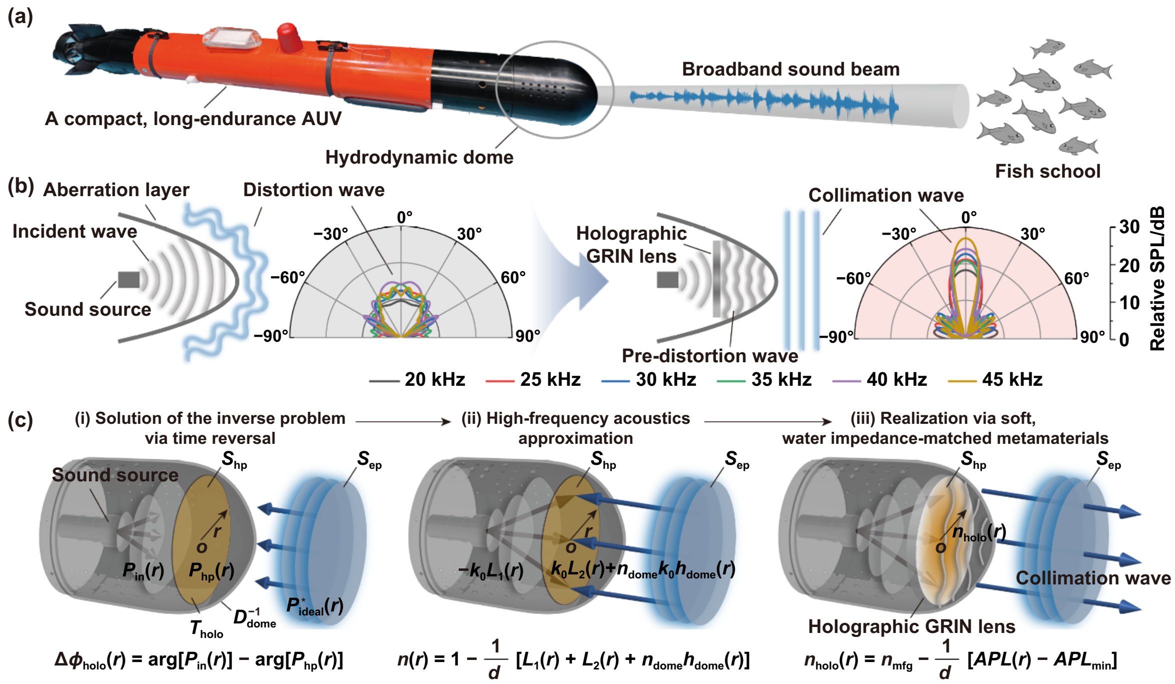

Figure 1. Principle and design process of the holographic gradient-index (GRIN) lens for aberration correction of an AUV's hydrodynamic dome. (a) Conceptual illustration of the AUV equipped with the proposed lens generating a collimated, broadband sound beam for long-range acoustic applications, such as fish school detection. (b) Simulated acoustic fields without (left) and with (right) the lens. The holographic lens corrects the severe wave aberration and frequency-dependent beam splitting caused by the dome, producing a single, high-intensity broadband collimated beam. (c) The three-step design methodology: (i) the required phase profile is calculated by solving the inverse problem via time reversal; (ii) this phase profile is converted to a theoretical refractive index profile using a high-frequency approximation; (iii) the profile is normalized and realized as a physical lens using soft metamaterials for practical manufacturing.

sound source level achieves more than 10 dB of reverberation suppression and a significant increase in the effective detection range. This work provides a new, passive pathway to overcome physical limitation in sonar design, paving the way for the next generation of high-performance, compact underwater sensing platforms.

2. Results

2.1. Broadband holographic design principle

As shown in Figure 1(c), consider a sound source located at position $\mathbf{r}_s$. The acoustic field reaching the holographic plane S_{hp} is governed by the free-space propagator $\mathcal{P}_{\mathrm{s}\rightarrow\mathrm{hp}}$. The effect of the designed holographic surface is modeled by the holographic transfer operator $\mathcal{T}_{\mathrm{holo}}$, followed by the AUV's dome represented by the aberration operator $\mathcal{D}_{\mathrm{dome}}$. Thus, the acoustic field at the emission plane S_{ep}, denoted by P_{e}, can be expressed as a sequential operation:

$$P_{\mathrm{e}}(\mathbf{r}_{\mathrm{ep}}) = \mathcal{D}_{\mathrm{dome}}{}^{\circ}\mathcal{T}_{\mathrm{holo}}{}^{\circ}\mathcal{P}_{\mathrm{s}\rightarrow\mathrm{hp}}[\mathrm{S}(\mathbf{r}_{\mathrm{s}})]. \tag{1}$$

The key nomenclature and parameter definitions in this work are summarized in Table S1. The aberration operator $\mathcal{D}_{\mathrm{dome}}$ is central to this theoretical framework. It is rigorously defined as an integral operator with the Green's function $G(\mathbf{r},\mathbf{r}')$ as its kernel, which characterizes the wave propagation under the full geometric and material boundary conditions of the AUV's dome. This Green's function satisfies the Helmholtz equation[41]:

$$\left[\nabla\cdot\left(\frac{1}{\rho(\mathbf{r})}\nabla\right)+\frac{\omega^2}{\rho(\mathbf{r})\,c^2(\mathbf{r})}\right]G(\mathbf{r},\mathbf{r}') = -4\pi\,\delta(\mathbf{r}-\mathbf{r}'). \tag{2}$$

Using this Green's function, the action of $\mathcal{D}_{\mathrm{dome}}$, which maps an arbitrary field P_{hp} from the holographic plane S_{hp} to the emission plane S_{ep}, can be formulated via the Kirchhoff–Helmholtz integral theorem:

$$P_{\mathrm{e}}(\mathbf{r}_{\mathrm{ep}}) = \mathcal{D}_{\mathrm{dome}}[P_{\mathrm{hp}}] = \int_{S_{\mathrm{hp}}}\left(P_{\mathrm{hp}}(\mathbf{r}_{\mathrm{hp}})\frac{\partial G(\mathbf{r}_{\mathrm{ep}},\mathbf{r}_{\mathrm{hp}})}{\partial n} - G(\mathbf{r}_{\mathrm{ep}},\mathbf{r}_{\mathrm{hp}})\frac{\partial P_{\mathrm{hp}}(\mathbf{r}_{\mathrm{hp}})}{\partial n}\right)\mathrm{d}S_{\mathrm{hp}}. \tag{3}$$

Here, $G(\mathbf{r}_{\mathrm{ep}},\mathbf{r}_{\mathrm{hp}})$ encapsulates all aberration effects induced by the dome, including phase distortion from acoustic path differences, amplitude modulation due to surface curvature, interfacial transmission, reflection, and diffraction. Given the system's complexity, a closed-form solution for $G(\mathbf{r}_{\mathrm{ep}},\mathbf{r}_{\mathrm{hp}})$ is generally intractable and must be computed numerically using the finite element method (FEM).

The goal is to determine a holographic transfer operator T_{holo} that can pre-compensate for these aberrations such that:

$$\mathcal{D}_{\mathrm{dome}}{}^{\circ}\mathcal{T}_{\mathrm{holo}}[P_{\mathrm{in}}] = P_{\mathrm{ideal}} \tag{4}$$

where P_{in} is the input field on the holographic plane and P_{ideal} is the desired collimated beam field at the emission plane. This is equivalent to finding a holographic output field $P_{\text{hp}} = \mathcal{T}_{\text{holo}}[P_{\text{in}}]$ such that:

$$P_{\text{hp}}(r_{\text{hp}}) = \mathcal{D}^{-1}_{\text{dome}}[P_{\text{ideal}}(r_{\text{ep}})]. \quad (5)$$

While this requires computing the inverse aberration operator $\mathcal{D}^{-1}_{\text{dome}}$, which is non-trivial due to the complexity of the kernel, the principle of time reversal provides a powerful solution[42,43]. For a lossless and reciprocal system, the inverse operator in the frequency domain corresponds to phase-conjugated back-propagation (Figure 1(c-i)).

To obtain the required holographic field P_{hp}, we proceed as follows: (i) define a phase-conjugated ideal source field $P^{*}_{\text{ideal}}(\mathbf{r})$ at the emission plane S_{ep}; (ii) simulate backward wave propagation through the dome structure, approximated using polynomial fits to the internal and external dome contours (Supplementary Discussion 1 and Figure S1); (iii) record the resulting complex pressure field at the holographic plane as $P_{\text{hp}}(\mathbf{r})$. The hologram surface is then designed to apply a phase-only modulation:

$$P_{\text{hp}}(\mathbf{r}) = P_{\text{in}}(\mathbf{r})\, e^{-j\Delta\phi_{\text{holo}}(\mathbf{r})}. \quad (6)$$

Taking the argument on both sides yields the required phase compensation:

$$\Delta\phi_{\text{holo}}(\mathbf{r}) = \arg[P_{\text{in}}(\mathbf{r})] - \arg[P_{\text{hp}}(\mathbf{r})]. \quad (7)$$

This phase shift compensates for the mismatch between the incident and desired output fields. It can be related to the physical parameters of the hologram, including the local thickness d and spatial refractive index $n(\mathbf{r})$ relative to water via: $\Delta\phi_{\text{holo}}(\mathbf{r}) = k_0 d[n(\mathbf{r}) - 1]$, where k_0 is the wavenumber in the background medium (water). Rearranging gives:

$$n(\mathbf{r}) = 1 + \frac{1}{k_0 d}\left(\arg[P_{\text{in}}(\mathbf{r})] - \arg[P_{\text{hp}}(\mathbf{r})]\right). \quad (8)$$

To facilitate a tractable design applicable over a broad bandwidth, we adopt the high-frequency approximation, where the phase accumulation is primarily determined by the acoustic path length L (Figure 1(c-ii)). For an outgoing diverging wave from the source, the forward-propagated phase is:

$$\arg[P_{\text{in}}(\mathbf{r})] = -k_0 L_1(\mathbf{r}) \quad (9)$$

where $L_1(\mathbf{r})$ represents the spatial distance from the source to the hologram plane. The backward phase accumulation through the dome is:

$$\arg[P_{\text{hp}}(\mathbf{r})] = k_0 L_2(\mathbf{r}) + n_{\text{dome}} k_0 h_{\text{dome}}(\mathbf{r}) \quad (10)$$

where n_{dome} is the acoustic refractive index of the material constructing the AUV's dome, $h_{\text{dome}}(\mathbf{r})$ is the thickness of the dome, and $L_2(\mathbf{r})$ represents the spatial distance from the hologram to the emission plane, excluding the dome. Thus, the desired refractive index profile of the hologram is

$$n(\mathbf{r}) = 1 - \frac{1}{d}[L_1(\mathbf{r}) + L_2(\mathbf{r}) + n_{\text{dome}} h_{\text{dome}}(\mathbf{r})]. \quad (11)$$

Importantly, this formulation is frequency-independent, enabling broadband functionality.

Only the relative phase shift across the aperture affects wavefronts. Hence, a constant offset can be subtracted without altering the wavefront shaping. To ensure manufacturability, we normalize the profile based on achievable refractive indices. Define the acoustical path length (APL) to be compensated:

$$APL(\mathbf{r}) = L_1(\mathbf{r}) + L_2(\mathbf{r}) + n_{\text{dome}} h_{\text{dome}}(\mathbf{r}). \quad (12)$$

Define the minimum required APL over the hologram surface as:

$$APL_{\text{min}} = \min_{\mathbf{r}}[APL(\mathbf{r})]. \quad (13)$$

Then, the practical refractive index profile $n_{\text{holo}}(\mathbf{r})$ is derived by anchoring the minimum value to a manufacturable baseline n_{mfg}, taken here as 1.54, and adjusting it based on relative path differences:

$$n_{\text{holo}}(\mathbf{r}) = n_{\text{mfg}} - \frac{1}{d}[APL(\mathbf{r}) - APL_{\text{min}}]. \quad (14)$$

This ensures that the hologram provides the necessary spatial variation for wave collimation, while all the refractive index values remain within the manufacturable bounds (Figure 1(c-iii)).

2.2. Physical realization of the holographic GRIN lens

For compact, long-endurance AUVs, the physical dimensions of any acoustic devices integrated into the vehicle's dome are critical design constraints. Correcting severe aberrations caused by hydrodynamic domes using a thin-type device is challenging because the low acoustic energy density of conventional underwater materials limits the phase shift achievable in compact structures[44]. Furthermore, to achieve high-energy transmission for long-range echo detection, excellent broadband acoustic impedance matching with water is required, a characteristic often compromised when the refractive index of functional materials is adjusted.

To overcome these limitations and realize the GRIN profile designed by our theory, we synthesized a soft metamaterial composed of tungsten micro-particles uniformly dispersed in a soft silicone elastomer matrix (Figure 2(a)). The silicone matrix (Ecoflex™ 00-30, Smooth-On Inc.) was selected because of its intrinsic flexibility, chemical robustness, and acoustic impedance compatibility with water. Micron-scale tungsten powder (1–5 µm diameter, T109164, Aladdin) served as the functional filler to modulate the

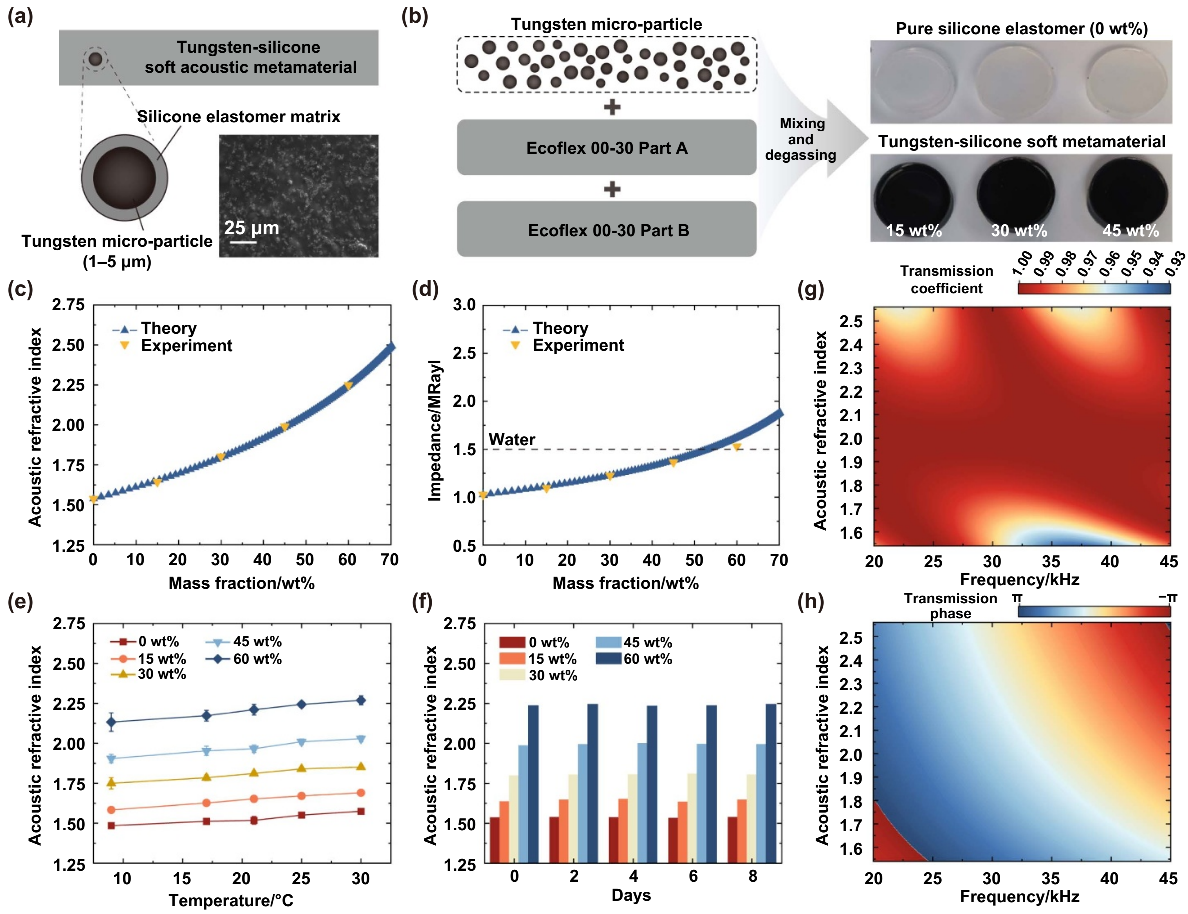

Figure 2. Fabrication process, characterization and environmental stability of the tungsten-silicone soft metamaterial. (a) Schematic of the microstructure, which consists of tungsten micro-particles (1–5 μm in diameter) embedded within a silicone elastomer matrix. Scanning electron microscopy (SEM) image of the fabricated tungsten-silicone soft metamaterial, showing the uniform dispersion of tungsten micro-particles (bright spots) within the silicone elastomer matrix. Scalebar, 25 μm. (b) The fabrication process involves mixing tungsten micro-particles with Ecoflex 00-30 Part A and Part B, followed by mixing and degassing. The resulting fabricated samples with 0 wt%, 15 wt%, 30 wt%, and 45 wt% tungsten are shown in the figure on the right. (c) and (d) Measured acoustic refractive index (c) and acoustic impedance (d) at 0.5 MHz of the composite as a function of the tungsten mass fraction (wt%). The experimental measurements (yellow triangles) are in excellent agreement with the theoretical model (blue triangle-marked dotted lines). The dashed line in (d) indicates the impedance of water for reference. (e) Measured effective refractive index as a function of water temperature, demonstrating good thermal stability. (f) Measured effective refractive index after prolonged immersion in artificial seawater, confirming long-term chemical and physical stability. (g) and (h) Numerically calculated amplitude (g) and phase (h) of the complex transmission coefficient for a single metamaterial pixel, plotted as a function of its effective refractive index and the operational frequency.

material's acoustic properties (Figure 2(b)). The composite was fabricated using a sequential molding and casting protocol. Firstly, precisely weighed quantities of the tungsten powder and silicone Part A were mechanically blended at high speed to achieve uniform dispersion and prevent particle agglomeration. Subsequently, silicone Part B was introduced and thoroughly mixed. This two-step approach is critical for preventing premature gelation, which could otherwise occur during the long mixing time required for the powder. The resulting slurry was then degassed under vacuum to remove entrapped air bubbles that are detrimental to the acoustic performance. Finally, the slurry was cast into a custom polytetrafluoroethylene (PTFE) mold, fabricated by precision computer numerical control (CNC) machining, and subjected to accelerated thermal curing at 60 °C for 3 hours. This rapid solidification inhibits the gravitational sedimentation of dense tungsten particles before the matrix fully cross-links. Scanning electron microscopy (SEM) confirmed the homogeneous distribution of the tungsten particles (Figures 2(a) and S2), validating the efficacy of our fabrication method.

The acoustic properties of this metamaterial can be accurately described using the Waterman–Truell multiple-scattering model[45]. This model describes wave propagation in a statistically homogeneous medium containing randomly distributed scatterers by relating the effective wavenumber to the ensemble-averaged forward- and backward-scattering amplitudes. Under the assumptions of an isotropic scatterer distribution and long-wavelength excitation, the effective wavenumber k_{eff} is expressed in terms of the single-scatterer forward-scattering amplitude $f(0)$ and backward-scattering amplitude $f(\pi)$:

$$\left(\frac{k_{\text{eff}}}{k_0}\right)^2 = \left[1+\frac{2\pi\eta_0 f(0)}{{k_0}^2}\right]^2 - \left[\frac{2\pi\eta_0 f(\pi)}{{k_0}^2}\right]^2. \quad (15)$$

Tungsten micro-particles, with a size smaller than 5 µm, are much smaller than the operational wavelength $\lambda\,(=c_0/f = 33\ mm,\ f = 45\ kHz)$, satisfying the long-wavelength condition, known as the Rayleigh scattering limit ($ka \ll 1$). In this regime, the scattering coefficients are dominated by the monopole, dipole, and quadrupole modes. By expressing the scattering amplitudes in terms of the mechanical properties, the effective wavenumber k_{eff} can be explicitly derived as

$$k_{\text{eff}}^2 = k_0^2\left(\frac{V_{\text{f}}\rho_1+(1-V_{\text{f}})\rho_0}{\rho_0}\right)\times\left(1-\left(\frac{3(K_1-K_0)}{3K_1+4G_0} - \frac{20G_0(G_0-G_1)}{G_0(9K_0+8G_0)+6G_1(K_0+2G_0)}\right)V_{\text{f}}\right) \quad (16)$$

where V_f is the volume fraction of scatterers, and the subscripts 0 and 1 denote the material parameters for the silicone matrix and tungsten scatterers, respectively. From the effective wavenumber, the effective sound velocity and refractive index are extracted using $n_{\text{eff}} = k_{\text{eff}}/k_0$. For consistency with the fabrication parameters, the theoretical data in Figure 2(c) is plotted as a function of mass fraction φ, which relates to the volume fraction via $\varphi = \rho_1 V_f/[\rho_1 V_f + \rho_0(1-V_f)]$. Detailed derivations are provided in Supplementary Discussion 2. Systematic characterization of the prepared samples validated the model. The experimentally measured effective refractive index was in good agreement with the theoretical values, confirming that the refractive index can be continuously tuned by controlling the tungsten mass fraction (Figure 2(c)). Validity analysis confirms that the Waterman–Truell model remains robust under the experimental mass fractions (Supplementary Discussion 3). Furthermore, theoretical generalization reveals that the design is robust against particle size randomness, as the effective medium response is preserved for polydisperse scatterers within the long wavelength limit (Supplementary Discussion 4). To evaluate the broadband performance, we characterized the acoustic refractive index of the tungsten-silicone soft metamaterial across the 0.5–2 MHz frequency range. The measured indices remain remarkably consistent, demonstrating negligible dispersion (Figure S3).

The wide refractive index range is achieved without compromising the acoustic transparency. As shown in Figure 2(d), although the acoustic impedance of this metamaterial also varies with tungsten content, it can still be almost perfectly matched to that of water (∼1.5 MRayl). Furthermore, experimentally measured attenuation coefficients confirm that the material exhibits low acoustic loss, with values remaining below 0.785 dB·cm^{-1} across the operational frequency band of 20–45 kHz (Figure S4 and Table S2). This impedance-matched and low-loss soft metamaterial provides the essential material foundation to accurately implement holographic design.

To assess the operational robustness of the metamaterial, its acoustic properties were characterized under simulated marine conditions. First, the effective refractive index was measured across a water temperature range of 9–30 °C, which is representative of the thermal variations encountered by AUVs, particularly when operating in surface waters or crossing thermoclines. The refractive index exhibits a slight, linear dependence on temperature, with a measured coefficient of +0.005 32 °C (Figure 2(e)). This variation is attributed mainly to the temperature-dependent changes in the sound speed of the silicone matrix, and the overall small coefficient confirms the device's excellent thermal stability based on the designed soft metamaterial. Furthermore, to evaluate its performance in saline environments, the samples were immersed in artificial seawater (3.5% salinity) for an 8-day period. The refractive index remained remarkably stable throughout the test (Figure 2(f)). This result demonstrates that the material maintains its physical integrity and acoustic stability upon seawater exposure. Such stability is a critical prerequisite for reliable performance during the long-duration underwater deployments required for modern AUVs.

Our designed holographic gradient lens can be conceptualized as an assembly of subwavelength pixels, each acting as a local phase modulator. The acoustic response of each pixel, modeled as a homogeneous slab of thickness d, is precisely described by its complex transmission coefficient T[41]:

$$T = \frac{2Z_n}{2Z_n\cos(k_{\text{L}}d)+i(Z_n^2+1)\sin(k_{\text{L}}d)} \quad (17)$$

where $Z_n = Z_L/Z_w$ is the normalized acoustic impedance of the lens material relative to water and k_L is the acoustic wavenumber within the lens. This fundamental relation dictates both the energy transmission efficiency, given by the amplitude $|T|$, and the imparted phase shift, given by the phase $\arg(T)$. We calculated these properties for our tungsten-silicone metamaterial using a fixed thickness of $d = 1.95$ cm, corresponding to the physical thickness of our fabricated lens. The theoretical transmission and phase maps derived from this equation are shown in Figures 2(g) and (h). The results confirm that near-total energy transmission ($|T| \approx 1$) is maintained across the broadband operational range due to the excellent impedance matching. Moreover, the parameter space spanning the operational frequencies and the material's achievable refractive indices provides full control over the transmission phase, covering the entire range from $-\pi$ to π (Figure 2(h)), which is essential for a broadband holographic design.

The translation of the holographic phase map into a physical structure is enabled by establishing a direct relationship between the required phase shift compensation and the material's local refractive index. The holographic GRIN lens is physically realized as a structure of discrete concentric rings, each assigned a specific, uniform refractive index (Figure 3(a)). The index value for each ring is determined by discretizing an ideal, continuous gradient-index profile that is designed to compensate for the dome's aberration (Figure 3(b)). This theoretical profile is generated from the required holographic phase map using the aforementioned

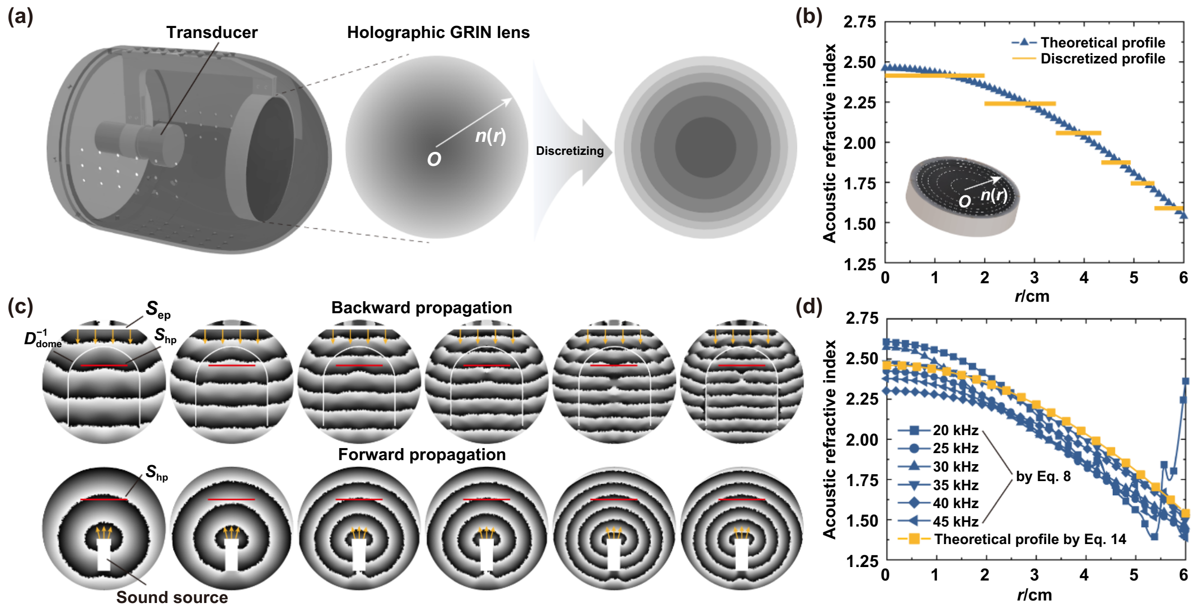

Figure 3. Realization of the holographic GRIN lens. (a) Schematic of the holographic GRIN lens. For practical fabrication, the continuously varying radial refractive index profile is discretized into a finite number of concentric rings, each with a uniform refractive index. (b) The required radial refractive index profile of the holographic lens calculated by the high-frequency approximation via Equation (14) (blue line) and its discretized version used for fabrication (orange bars). Inset: a photo of the lens. (c) Holographic phase extraction via simulated acoustic fields. The top row simulates a plane wave launched from an emission plane propagating backward through the aberrating dome. The bottom row simulates a wave from the forward-propagating sound source. The phase difference between these two fields at the designated holographic plane (red line) yields the required phase compensation profile. (d) Comparison between the required refractive index profile derived from the complete time-reversal phase compensation (blue line for different frequencies, calculated via Equation (8)) and the simplified profile obtained via the high-frequency approximation (yellow line, calculated via Equation (14)). The agreement across the broadband range validates the approximation used in the lens design.

high-frequency approximation (Equation (14)). The detailed acoustic parameters for each discretized ring of the holographic GRIN lens are listed in Table S3. In our design, the holographic GRIN lens employs an equal refractive index interval discretization to balance fabrication feasibility and modulation precision. The maximum accumulated phase deviation across the lens thickness, arising from the discrepancy between the continuous and discrete refractive index distributions, remains limited to 0.156π over the effective aperture within the operating frequency range of 20–45 kHz (Figure S5). This ensures that the acoustic response of the discretized lens is essentially equivalent to that of the ideal continuous design. Additionally, concentric rings were fabricated via a radial step-wise co-curing process utilizing the same silicone matrix. By casting each subsequent ring onto the semi-cured interface of the preceding ring, this method facilitates strong cross-linking between layers. Consequently, the rings fuse into a monolithic elastomer rather than a laminated assembly. Such seamless integration, together with the gradual impedance variation across the lens, effectively suppresses interfacial reflections and minimizes boundary coupling effects.

The design originates from our holographic phase extraction method. By calculating the phase difference at the holographic plane between a backward-propagating plane wave and a forward-propagating wave from the source, the precise phase compensation is obtained (Figure 3(c)). The accuracy of this phase-only modulation is further guaranteed by the soft metamaterial's sufficiently low intrinsic loss (Figure S4), which minimizes amplitude-induced distortions and justifies the lossless approximation used in the time reversal design. To assess the validity of the high-frequency approximation, its resulting GRIN profile was compared to one derived from the complete time-reversal phase compensation formula (Equation (8)). As shown in Figure 3(d), the refractive index profiles calculated by both methods exhibit good consistency across the entire 20–45 kHz operating bandwidth. We further calculated the phase deviation between the two methods (Figure S6). The maximum phase deviation remains below approximately 0.25π (corresponding to a path difference $< \lambda/8$), with a standard deviation below 0.095π. This indicates that the high-frequency approximation provides a sufficiently accurate phase design rule within the considered frequency band.

2.3. Broadband aberration-free collimation

To validate the performance of the fabricated holographic GRIN lens, we performed full-wave simulations and underwater experiments (Figure 4). First, we examined the near-field acoustic pressure distributions (Figure 4(a)). The simulation results (main figure) are highly consistent with the experimental results (inset). Without the lens (top row), the dome severely scatters and distorts the sound field, resulting in an irregular and highly divergent wavefront. Upon introducing the holographic lens (bottom row), a significant change occurred. The lens precisely compensated for the phase

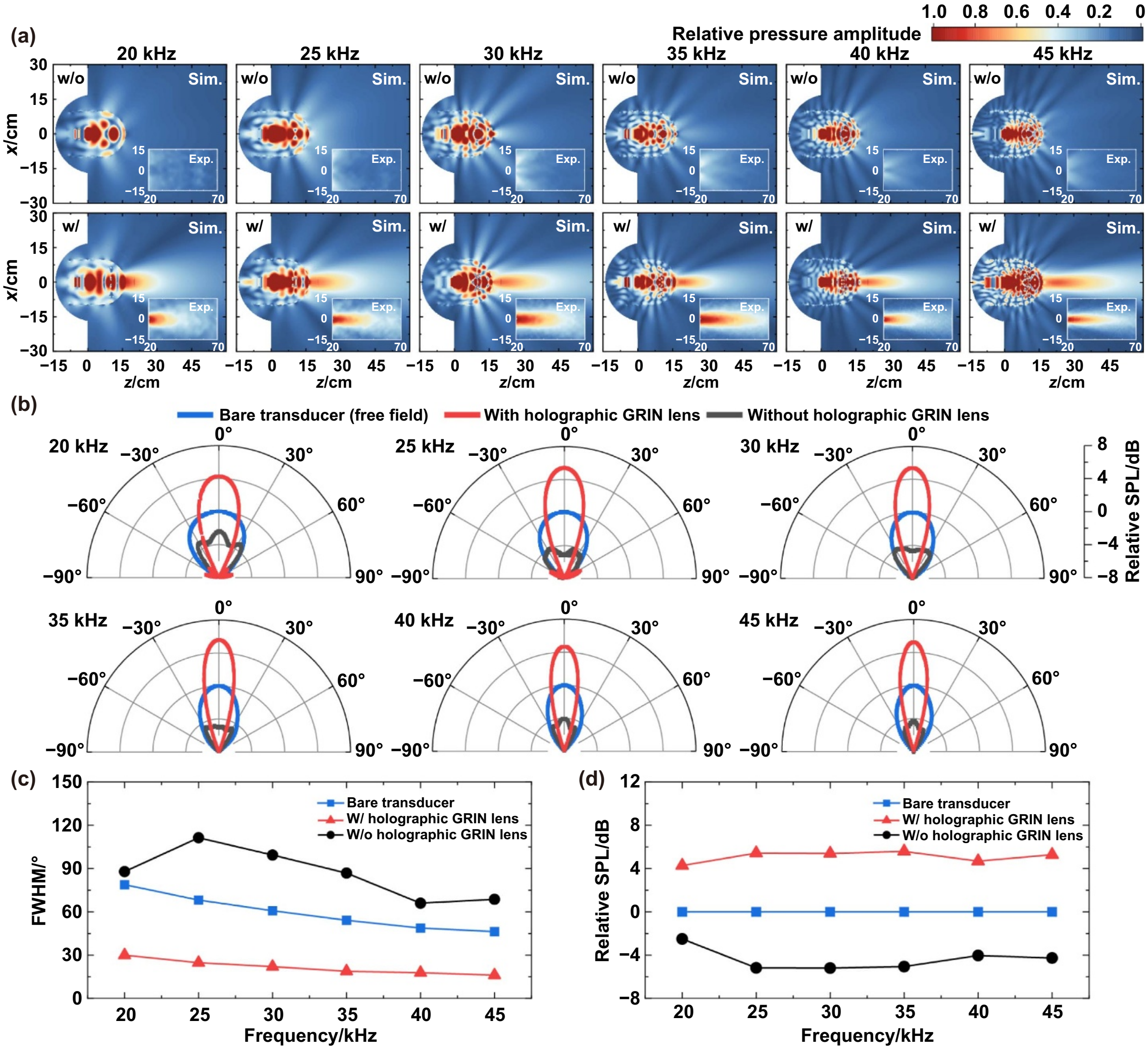

Figure 4. Numerical and experimental validation of broadband aberration correction and collimation. (a) Simulated (main panels) and experimentally measured (insets) acoustic pressure distributions from 20 kHz to 45 kHz. The top row shows the distorted wavefronts produced by the aberrating AUV's dome. The bottom row shows the highly collimated planar wavefronts achieved after introducing the holographic GRIN lens. (b) Far-field radiation patterns at different frequencies, measured at a distance of 2 m from the source, comparing three configurations: the bare transducer in a free field, the transducer with the aberrating dome only, and the complete system corrected by the holographic GRIN lens. (c) Full width at half maximum (FWHM, or −3 dB) beamwidth as a function of frequency. (d) On-axis relative source pressure level (SPL) as a function of frequency, referenced to the bare transducer at 0 dB.

aberration caused by the dome, reshaping the scattered waves into highly collimated waves and maintaining their coherence over long distances. This highly directional sound beam is a clear indicator of successful aberration correction and consistently observed across the entire 20–45 kHz operating frequency band.

Next, we analyzed the far-field radiation patterns at a distance of 2 m from the sound source (Figure 4(b)). As a reference, the bare transducer radiates with a broad, low-directivity beam (blue curve). The introduction of the aberrating dome further degrades performance, resulting in a diffuse and irregular beam profile (black curve). In contrast, the addition of our holographic lens guides the acoustic energy into a clean, highly directive beam with significantly suppressed sidelobes (red curves). These experimental radiation patterns are in good agreement with our full-wave simulation results (Figure 1(b)). This indicates that the near-field correction effectively translates into an exceptional improvement in far-field directivity, which is critical for long-distance sensing and imaging.

A quantitative analysis of broadband performance was then conducted. Figure 4(c) shows the relationship curve between the full width at half maximum (FWHM) of the beamwidth (also denoted as the −3 dB beamwidth) and the frequency. The −3 dB beamwidth of the bare transducer (blue curve) is wide, exceeding 46°, whereas the baseline configuration with the aberrating dome present (black curve) further degrades the directivity, broadening the beam profile to exceed 65°. However, the holographic lens provides an approximately 4-fold reduction in beamwidth, consistently maintaining a

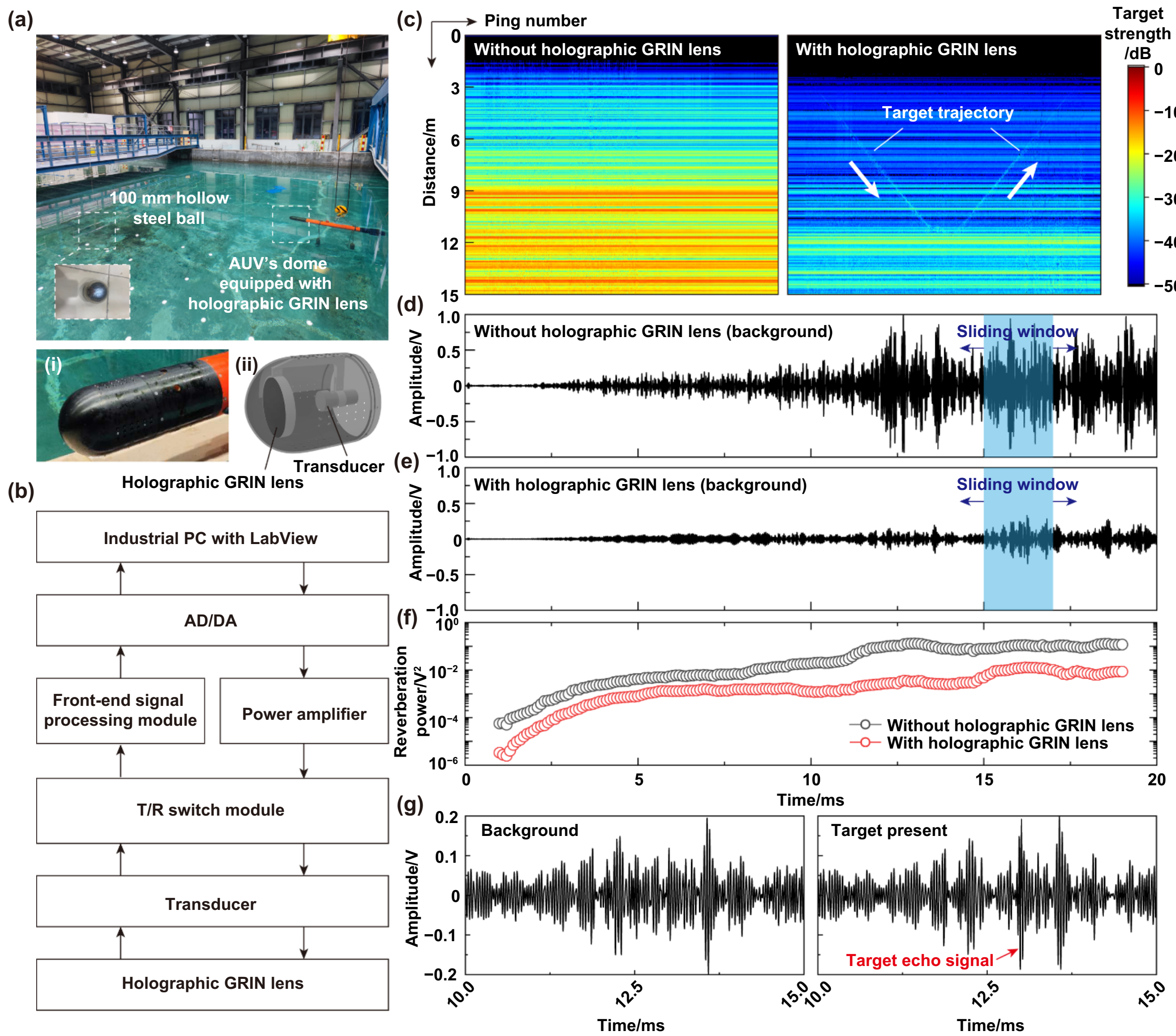

Figure 5. System demonstration of enhanced underwater echo detection in a water tank. (a) Photograph of the experimental setup in the water tank. A hollow steel ball (100-mm diameter) serves as the target. Insets show (i) the AUV's dome and (ii) a schematic of the dome equipped with the holographic GRIN lens. (b) Block diagram of the underwater echo-detection system constructed for the experiment. (c) Waterfall plots of target strength over time for multiple pings. Each plot is constructed by stacking the echo profile from every consecutive ping as a vertical line, with the echo strength mapped to a color scale. Left: without the lens. Right: with the lens. (d) A representative time-domain signal recorded by the system without the lens, showing the target echo completely submerged in background reverberation. (e) Time-domain signal of the background field measured with the lens installed but without the target present. (f) Quantitative analysis of reverberation power over time, calculated from the signals in (d) and (e) using a sliding window. (g) Echo signal when the lens is installed. The signal from the background alone (left) is compared to the signal with the target present (right), where the target echo signal is now clearly distinguishable.

narrow 16°–30° profile across the entire operating frequency band. A downward trend in the beamwidth with increasing frequency is also apparent, a behavior consistent with the fundamental diffraction limit ($\theta \approx \lambda/D$). We also evaluated the on-axis source pressure level (SPL) enhancement based on the experimental data (Figure 4(d)). The aberrating dome causes a significant power reduction, with the SPL decreasing by approximately 4 dB relative to the bare transducer (0 dB reference). The holographic lens not only compensates for this loss but also provides an additional ∼6 dB of gain, resulting in a total SPL enhancement exceeding 10 dB at the center frequency. This demonstrates the lens's ability to efficiently redirect acoustic energy along the desired axis.

2.4. Enhanced underwater echo detection

To demonstrate the practical utility of our holographic lens, we constructed and tested a complete underwater echo-detection system, first in a water tank (27 m × 15 m × 2.5 m). Figure 5(a) shows a photograph of the experimental setup, where a 100-mm-diameter hollow steel ball serves as a moving target. The detection system is equipped within an AUV's forebody, with the dome equipped with our holographic GRIN lens. The system is controlled by an industrial PC running custom software based on LabVIEW. Signal generation and data acquisition are handled by an analog-to-digital/digital-to-analog (AD/DA) converter and a transceiver unit that includes a front-end signal processing module and a T/R switch module (Figure 5(b)).

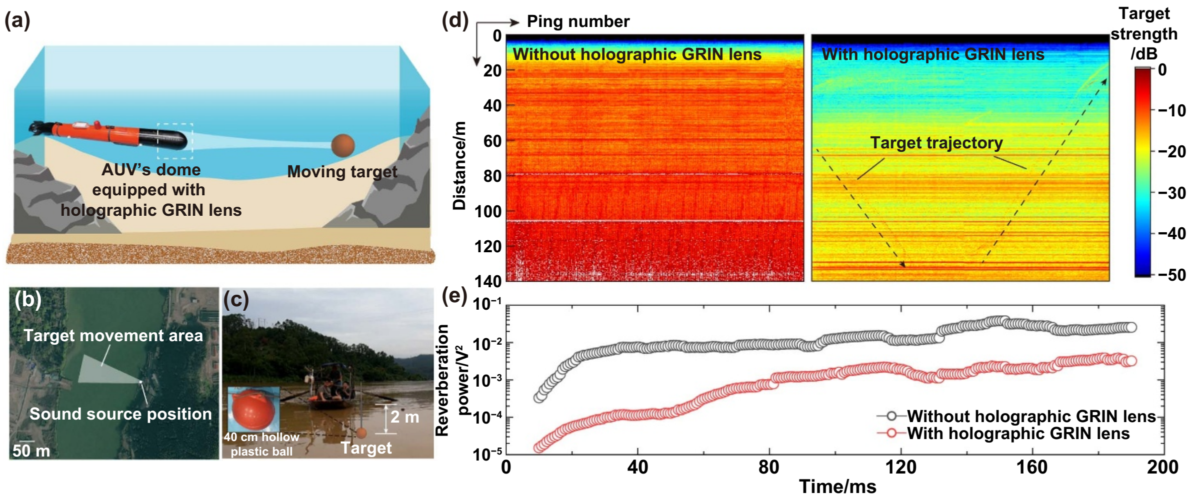

Figure 6. System demonstration of enhanced underwater echo detection in the open-water field. (a) Schematic of the echo detection experiment with the AUV's dome equipped with the holographic GRIN lens in an open-water field. (b) Map of the field trial site on the Jiulong River in Zhangzhou, China. (c) A hollow plastic ball, submerged at a 2-m depth and towed by a boat, was used as a moving target. (d) Waterfall plots of target strength over time for multiple pings. Left: without the lens, the target's trajectory is completely obscured by strong environmental reverberation. Right: with the lens, reverberation is suppressed, and the target's trajectory is clearly resolved. (e) The reverberation power measured with the lens and without the lens, calculated using a 20-ms sliding window.

In the test, we used a broadband linear frequency-modulated (LFM) chirp signal (20–40 kHz) to detect the target.

We first confirmed that the holographic GRIN lens provides excellent broadband performance without introducing frequency distortion (Supplementary Discussion 5 and Figure S7). The results show that the fundamental structure of the LFM pulse is well-preserved in the time domain, while its corresponding acoustic signal spectrum accurately reproduces the input electrical signal spectrum across the entire operational band. This verification confirms the lens's suitability for modern broadband sonar systems.

The overall performance enhancement is visualized in the waterfall plots of target strength over multiple pings, as shown in Figure 5(c). Without the lens, strong and persistent reverberation from the tank boundaries completely obscures the weak echo from the target, making detection impossible. In contrast, when the holographic lens is installed, this background reverberation is significantly suppressed, allowing the target's trajectory to be clearly resolved up to a distance of 11 m. A detailed analysis of the time-domain echo signal from a single-pulse compression reveals the physical origin of this improvement. Figure 5(d) shows a representative signal from the system without the lens, where any potential target echo is completely submerged in the strong reverberation background. For comparison, we recorded the background reverberation with the lens installed but without the target present; this significantly quieter background is shown in Figure 5(e). To quantify the reverberation suppression, we performed an analysis using a 2-ms sliding window (represented by the blue shaded boxes in Figures 5(d) and (e)) to calculate the reverberation power P_{reverb} from the mean squared amplitude. The results clearly demonstrate that the reverberation power is substantially lower when the lens is equipped (Figure 5(f)), resulting in an average reduction of 10.41 dB, as calculated with

$$R_{\text{p}}\left(\text{dB}\right) = 10\log_{10}\left(\frac{P_{\text{reverb\_with\_lens}}}{P_{\text{reverb\_without\_lens}}}\right). \qquad (18)$$

Consequently, when equipped with the lens, the target's echo can be clearly distinguished from the suppressed background within a single ping (Figure 5(g)).

To validate this performance in a real-world environment, we conducted an open-water field trial on the Jiulong River (Figure 6). Figure 6(a) illustrates the forward detection concept being tested. The trial site map is shown in Figure 6(b), together with the corresponding bathymetric profile (Figure S8), which reveals a U-shaped riverbed characterized by a central channel approximately 15 m deep and shallow banks with depths below 5 m. During the experiment, the AUV was deployed in the shallow region near the riverbank and maintained a fixed heading, directing the acoustic beam across the channel toward a predefined detection area. This complex bathymetry creates a challenging environment where a wide acoustic beam inevitably interacts with both the water surface and the riverbed at longer ranges, causing severe multipath reverberation. A hollow plastic sphere was submerged at a 2-m depth and towed by a boat, serving as a moving target (Figure 6(c)). Throughout the measurement process, the target remained within the main-lobe coverage of the acoustic beam.

The field trial results corroborated the laboratory findings, demonstrating the lens's robustness in a complex environment. The waterfall plots of the target strength again show a significant improvement (Figure 6(d)). Without the lens, the target's trajectory is completely obscured by strong environmental and boundary reverberation. After being equipped with the holographic lens, the reverberation is substantially reduced, and the target's trajectory becomes clearly visible. This improvement was quantified by calculating the reverberation power with and without the lens using a 20-ms sliding window (Figure 6(e)). The analysis confirms consistent and substantial reverberation suppression, with an average reduction of 11.98 dB. This demonstration in a challenging, open-water environment further provides strong evidence of our approach's practical applicability for enhancing echo detection performance.

This significant improvement in the effective detection range is driven by three synergistic physical mechanisms. Firstly, as quantified in the previous section, the lens increases the on-axis source pressure level (SPL) by more than 10 dB, ensuring that more acoustic energy acts on the target, thereby enhancing the echo signal itself. Secondly, based on the principle of reciprocity, the lens enhances the system's receiving sensitivity along the main lobe, further amplifying the received target echo. Finally, the directive beam significantly reduces the scattering energy of the boundaries, resulting in a reduction in background reverberation by over 10 dB. The combination of the stronger target signal and the quieter background leads to a substantial improvement in the signal-to-reverberation ratio, which enables reliable, long-range detection.

3. Discussion

Our work demonstrates a paradigm shift in correcting severe aberrations in compact sonar systems, transitioning from active electronic or computational methods to passive, soft material-based solutions. We have theoretically introduced and experimentally validated a passive, soft, and water-impedance-matched holographic GRIN lens that can simultaneously correct severe dome-induced aberrations and collimate a weakly directional sound wave into a highly directive beam. This multi-dimensional performance enhancement includes a $>$10 dB increase in the on-axis source level, a $\sim$4-fold reduction in the beamwidth, and an $\sim$11 dB suppression of reverberation, with all improvements achieved across a wide bandwidth. This can translate directly into a substantial enhancement of an AUV's operational capabilities, enabling the detection of smaller or stealthier targets at greater distances or, alternatively, allowing for a significant reduction in transmit power to extend mission endurance. Our approach offers a new and practical pathway to overcome the physical limitations associated with long constrained compact underwater sensing systems.

Compared with existing technologies, our approach has distinct advantages. The passive and compact design greatly reduces the SWaP-C metrics and complexity associated with large phased-array sonars, enabling the integration of high-performance acoustic systems into small, long-endurance AUV platforms. Despite the lack of dynamic beam steering capabilities of active reconfigurable metamaterials, our passive and robust solution is simpler and inherently broadband, making it more suitable for long-term reliable operation in harsh, energy-constrained underwater environments. Furthermore, unlike traditional rigid acoustic lenses, our soft GRIN lens, designed using the principles of time-reversal and high-frequency approximations, enables both broadband wavefront shaping and high acoustic transparency—a combination difficult to achieve with conventional solid bulk elements.

While our results demonstrate the metamaterial's robustness under key environmental conditions, its application in complex marine environments warrants further consideration. We have established that the material's refractive index is relatively stable across principal oceanic temperature zones and that its acoustic properties are unaffected by short-term seawater immersion, showing no signs of significant water absorption, swelling, or degradation (Figure S9). This stability is consistent with the inherent hydrophobicity of the silicone matrix; its low surface energy resists water ingress and contributes to the composite's enhanced corrosion resistance[46,47]. The effect of hydrostatic pressure, which increases with operational depth, is a critical consideration for underwater deployment. Owing to the near incompressibility of the silicone matrix (Poisson's ratio $\approx$ 0.5), its macroscopic isotropy, and the absence of internal voids, the soft lens is able to transmit hydrostatic pressure uniformly throughout the material, maintaining its structural integrity without significant volume compression or structural buckling. Furthermore, within the typical operational depth range of underwater vehicles, the impact of hydrostatic pressure on the sound speed of the tungsten-silicone soft metamaterial could be negligible. A detailed quantitative estimation of the acoustic stability under hydrostatic pressure is provided in Supplementary Discussion 6. To fully qualify the material for long-term deployment, future investigations will focus on its long-term chemical stability and corrosion resistance, particularly at the tungsten−silicone interface[48]. Furthermore, the material's response to marine biofouling warrants a dedicated study to ensure its performance and longevity under realistic oceanic conditions[49,50].

The molding and casting method employed in this study is a mature, cost-effective, and readily scalable manufacturing process. By using large, multi-cavity molds, it is easily scalable to decimeter-scale apertures and batch production of the lenses can be achieved to meet the demands of applications such as AUV swarms. While molding is ideal for scalable production, multi-material additive manufacturing (AM) offers a transformative pathway toward fabricating lenses with more sophisticated features, such as truly continuous gradient-index profiles[51,52]. Techniques such as direct ink writing (DIW) are particularly well-suited for depositing the viscous, particle-laden composite slurries used in this work[53,54]. By precisely controlling the local volumetric ratio of different composite inks—for instance, those with high and low refractive indices—during the printing process, AM can fabricate lenses with continuous GRIN profiles, thereby eliminating the step-like approximation errors inherent to discretized structures.

The significance of this work extends beyond AUV sonar, as the design paradigm—utilizing a holographic GRIN lens to compensate for broadband aberrations—is broadly applicable and extensible. It can be adapted for more complex asymmetric aberration correction or be applied to other wave domains, such as high-precision medical ultrasound through the human ribs or skulls[55–59], high-resolution non-destructive testing of curved industrial components[60–62], or even for shaping sound fields in architectural acoustics[63,64]. Moreover, advanced inverse-design and optimization algorithms can generate holographic profiles for more complex acoustic fields[65–68]. By applying mechanical deformation or integrating stimuli-responsive materials, dynamic beam control can be achieved, enabling functionalities such as beam steering or tunable focusing to further expand the acoustic sensing and communication capabilities[69–72]. Therefore, this study not only provides a solution for a critical challenge in underwater acoustics but also establishes a new and versatile design platform for advanced wavefront engineering.

4. Methods

4.1. Numerical modeling

The holographic design and performance validation were guided by three-dimensional (3D) numerical modeling performed using the commercial finite-element software COMSOL Multiphysics (Figure S10). The versatile design theory was first implemented to calculate the required phase profile, which was then converted into a gradient-index (GRIN) map for the 3D lens model. For performance validation, 3D full-wave simulations were conducted, which included calculations of both the near and far acoustic fields. The computational domain consisted of the acoustic device (dome and/or lens) and the surrounding water, truncated by a perfectly matched layer (PML) to emulate a free-field radiation condition. The water domain and the soft metamaterial lens were governed by the pressure acoustics module, whereas the AUV's dome (HN660-200, Tianhe Maritime Technologies), composed of Al6063, was modeled using the solid mechanics module. An acoustic–structure boundary coupling condition was applied at all fluid–solid interfaces. The material parameters for the tungsten–silicone composite were based on our experimental characterization results. The mesh size was set to be smaller than one-sixth of the shortest acoustic wavelength to ensure computational accuracy. The results presented in the main text, such as the acoustic pressure distribution in Figure 4(a), represent a 2D cross-section (x-z plane) of the full 3D simulation results.

4.2. Metamaterial characterization

The acoustic properties of the fabricated composites were characterized using an insert-substitution method. Cylindrical samples were positioned between two ultrasonic transducers in a water tank. The sound velocity was calculated from the time-of-flight difference of an ultrasonic pulse with and without the sample, from which the acoustic refractive index was derived. The acoustic impedance was calculated as the product of the measured density and sound velocity. To assess the material's environmental stability, these acoustic measurements were repeated under controlled conditions. For temperature-dependent characterization, the experimental setup was placed in a thermal bath. Measurements were performed across a range of 9–30 °C, ensuring that the system reached thermal equilibrium before data acquisition at each temperature point. For the seawater stability test, the samples were fully immersed in artificial seawater (3.5% salinity) and maintained at a constant room temperature. Their acoustic properties were then measured periodically. The microstructure and particle dispersion were verified using a scanning electron microscope (SEM).

4.3. Underwater acoustic field mapping

The near-field pressure distributions were mapped in a water tank (2 m × 1 m × 1 m) (Figure S11). A piston transducer (WTP30, Suzhou Acoustic Origin Transducer Corporation) served as the acoustic source, driven by a signal generator (Tektronix AFG 31022) and a power amplifier (ATA-L8, Aigtek), emitting a 5-cycle sinusoidal burst signal. The acoustic field was scanned by a hydrophone (RHC-7) mounted on a 3D motorized stage with a spatial resolution of 1 cm. The received signals were directly digitized by a digital oscilloscope.

The far-field radiation patterns were measured in a large water tank (27 m × 15 m × 2.5 m) to minimize boundary reflections and allow clear separation of the direct wave. Measurements were conducted at a distance of 2 m from the source over a 180-degree arc.

4.4. Target detection experiment

The system-level echo detection demonstration was performed using an AUV (HN660-200, Tianhe Maritime Technologies). The experimental hardware comprised a host computer, an AD/DA converter module, a power amplifier, a transceiver, which included a front-end signal processing circuit, and a transmit/receive (T/R) switch module. The system's operation was controlled by custom software developed on the NI LabVIEW platform.

During transmission, the host computer directs the AD/DA module to generate the analog waveform of a broadband linear frequency-modulated (LFM) chirp signal (20–40 kHz). Simultaneously, the T/R switch is set to the transmit state, allowing the signal to be amplified and used to drive the transducer, which radiates the acoustic pulse into the water to detect the moving target (100-mm-diameter hollow steel ball and 40-cm-diameter hollow plastic ball). Immediately after transmission, the T/R switch is set to the receive state. The returned echo, captured by the transducer, is converted into an electrical signal, which is then amplified and filtered by the front-end processing circuit. This conditioned analog signal is then digitized by the AD/DA module and transferred to the host computer for signal processing.

In software, the received signal is cross-correlated with the transmitted signal (matched filtering) to achieve pulse compression. The target strength is then calculated by compensating for the transmission loss, a process governed by the active sonar equation. The resulting waterfall plots of target strength over time for multiple pings were used to visualize the target's trajectory.

For the purpose of direct comparability, the experimental conditions were held constant across all trials. Key system parameters, including the transducer's transmission power and front-end signal processing settings, remained unchanged, isolating the holographic lens as the sole variable under investigation.

Acknowledgments

This work was supported by the National Key R&D Program of China (2024YFD2401402), the National Natural Science Foundation of China (12561160121 and 12411530074), the open fund of National Key Laboratory of Science and Technology on Underwater Acoustic Antagonizing (JCKY2025207CH06), the Smart Bay Area Observation and Big Data Analysis System Project, and the Jiangsu Provincial Joint Research Consortium for Key Deep-Sea Communication and Detection Technologies Project. The authors thank X. Xu from the College of Ocean and Earth Sciences, Xiamen University, for assisting with the target detection experiments.

Author contributions

J. Zhang and Y. Zhang designed the research. Y. Zhang and Z. Song supervised the project. J. Zhang and S. Liu performed the simulations. N. Zhou performed the material fabrication. J. Zhang, C. Yang, S. Liu, N. Zhou, Z. Bu, W. Zheng, and F. Zhang performed the experiments. J. Zhang wrote the manuscript. All the authors contributed to the analysis and discussion of the data.

Conflict of interests

The authors declare that they have no competing interests.

ORCID iD

Yu Zhang 0000-0001-6183-0612

References

[1] Wynn R B et al. 2014. Autonomous Underwater Vehicles (AUVs): their past, present and future contributions to the advancement of marine geoscience. *Mar. Geol.* **352**, 451–468.

[2] Lavimi R, Le Hocine A E B, Poncet S, Marcos B and Panneton R. 2024. Hull shape optimization of autonomous underwater vehicles using a full turbulent continuous adjoint solver. *Ocean Eng.* **312**, 119256.

[3] Sener M Z and Aksu E. 2022. The effects of head form on resistance performance and flow characteristics for a streamlined AUV hull design. *Ocean Eng.* **257**, 111630.

[4] Gao T, Wang Y X, Pang J Y and Cao J. 2016. Hull shape optimization for autonomous underwater vehicles using CFD. *Eng. Appl. Comput. Fluid Mech.* **10**, 599–607.

[5] Dmochowski J, Benesty J and Affes S. 2009. On spatial aliasing in microphone arrays. *IEEE Trans. Signal Process.* **57**, 1383–1395.

[6] Chen A, Xia Y-F, Chen Z-X, Su H-J, Liu -J-J, Yang J, Zhu X-F, Liang B and Cheng J-C. 2025. Dynamic and high-precision sound manipulation by acoustic metamaterial-empowered phased arrays. *Adv. Funct. Mater.* **35**, 2425833.

[7] Bureau F, Denis L, Coudert A, Fink M, Couture O and Aubry A. 2025. Ultrasound matrix imaging for 3D transcranial in vivo localization microscopy. *Sci. Adv.* **11**, eadt9778.

[8] Bureau F, Robin J, Le Ber A, Lambert W, Fink M and Aubry A. 2023. Three-dimensional ultrasound matrix imaging. *Nat. Commun.* **14**, 6793.

[9] Lambert W, Cobus L A, Robin J, Fink M and Aubry A. 2022. Ultrasound matrix imaging—Part II: the distortion matrix for aberration correction over multiple isoplanatic patches. *IEEE Trans. Med. Imaging* **41**, 3921–3938.

[10] Lambert W, Cobus L A, Frappart T, Fink M and Aubry A. 2020. Distortion matrix approach for ultrasound imaging of random scattering media. *Proc. Natl Acad. Sci. USA* **117**, 14645–14656.

[11] Liu Z Y, Zhang X, Mao Y, Zhu Y Y, Yang Z, Chan C T and Sheng P. 2000. Locally resonant sonic materials. *Science* **289**, 1734–1736.

[12] Ma G C and Sheng P. 2016. Acoustic metamaterials: from local resonances to broad horizons. *Sci. Adv.* **2**, e1501595.

[13] Dong E Q, Cao P, Zhang J, Zhang S, Fang N X and Zhang Y. 2023. Underwater acoustic metamaterials. *Natl Sci. Rev.* **10**, nwac246.

[14] Ge H, Yang M, Ma C, Lu M-H, Chen Y-F, Fang N and Sheng P. 2018. Breaking the barriers: advances in acoustic functional materials. *Natl Sci. Rev.* **5**, 159–182.

[15] Wang N Y, Huang S, Zhou Z, Tsai D P, Zhu J and Li Y. 2025. Seven-octave ultrabroadband metamaterial absorbers via quality-factor-weighted mode density modulation. *Natl Sci. Rev.* **12**, nwaf199.

[16] Ellouzi C, Aghdasi F, Zabihi A, Miri A K and Shen C. 2025. Versatile standing wave generation between arbitrarily oriented surfaces using acoustic metasurface deflectors and retroreflectors. *Adv. Intell. Syst.* **7**, 2400474.

[17] Wang X, Dong R, Li Y and Jing Y. 2023. Non-local and non-Hermitian acoustic metasurfaces. *Rep. Prog. Phys.* **86**, 116501.

[18] Zhong J-X, Ji J, Xia X, Heo H and Jing Y. 2025. Audible enclaves crafted by nonlinear self-bending ultrasonic beams. *Proc. Natl Acad. Sci. USA* **122**, e2408975122.

[19] Liu J J, Li Z, Liang B, Cheng J-C and Alù A. 2023. Remote water-to-air eavesdropping with a phase-engineered impedance matching metasurface. *Adv. Mater.* **35**, 2301799.

[20] Zhou P, Jia H, Bi Y, Yang Y, Yang Y, Zhang P and Yang J. 2023. Water–air acoustic communication based on broadband impedance matching. *Appl. Phys. Lett.* **123**, 191701.

[21] Huang Z D et al. 2021. Lotus metasurface for wide-angle intermediate-frequency water–air acoustic transmission. *ACS Appl. Mater. Interfaces* **13**, 53242–53251.

[22] Liu J J, Wang W, Zhao C, Zhou Y, Zhang H, Liang B, Qiu C-W and Cheng J-C. 2023. Static passive meta-sonar for dynamic sound beam scanning. *Sci. Bull.* **68**, 1862–1866.

[23] Su C X, Dong E, Gao Z, Zhang J, Zhang F, Yang C, Liu S, Wang Z, Fang N X and Zhang Y. 2025. Holographic sonar imaging via soft meta-structures. *Device* **3**, 100718.

[24] Zeng L-S, Lin Z-B, Li Z-L, Yang Y, Hu Y, Chen Z, Peng Y-G, Ma T, Zheng H-R and Zhu X-F. 2025. High-resolution manifold acoustic holography based on high-pixel-array binary metasurfaces. *Adv. Mater.* **37**, 2420229.
[25] Melde K, Mark A G, Qiu T and Fischer P. 2016. Holograms for acoustics. *Nature* **537**, 518–522.
[26] Zhang J, Tian Y, Cheng Y and Liu X. 2020. Acoustic holography using composite metasurfaces. *Appl. Phys. Lett.* **116**, 030501.
[27] Li Z-L et al. 2023. Decorated bacteria-cellulose ultrasonic metasurface. *Nat. Commun.* **14**, 5319.
[28] Xie S H, Ma H, Cao J, Mo F, Cheng Q, Li Y and Hao T. 2024. Refined acoustic holography via nonlocal metasurfaces. *Sci. China: Phys. Mech. Astron.* **67**, 274311.
[29] Assouar B, Liang B, Wu Y, Li Y, Cheng J-C and Jing Y. 2018. Acoustic metasurfaces. *Nat. Rev. Mater.* **3**, 460–472.
[30] Fan X D, Zhu Y, Li N, Weng C and Assouar B. 2023. Acoustic metaholograms for encrypted information transmission. *Phys. Rev.Appl.* **20**, 044048.
[31] Fan S-W, Zhu Y, Cao L, Wang Y-F, Li Chen A, Merkel A, Wang Y-S and Assouar B. 2020. Broadband tunable lossy metasurface with independent amplitude and phase modulations for acoustic holography. *Smart Mater. Struct.* **29**, 105038.
[32] Dong E Q et al. 2025. Soft metalens for broadband ultrasonic focusing through aberration layers. *Nat. Commun.* **16**, 308.
[33] Jiménez-Gambín S, Jiménez N, Benlloch J M and Camarena F. 2019. Holograms to focus arbitrary ultrasonic fields through the skull. *Phys. Rev. Appl.* **12**, 014016.
[34] Jiménez-Gambín S, Jiménez N and Camarena F. 2020. Transcranial focusing of ultrasonic vortices by acoustic holograms. *Phys. Rev.Appl.* **14**, 054070.
[35] Shen C et al. 2014 Anisotropic complementary acoustic metamaterial for canceling out aberrating layers. *Phys. Rev.* **4**, 041033.
[36] Li L C, Diao Y, Wu H and Jiang W. 2022. Complementary acoustic metamaterial for penetrating aberration layers. *ACS Appl. Mater. Interfaces* **14**, 28604–28614.
[37] Craig S R, Welch P J and Shi C. 2020. Non-hermitian complementary acoustic metamaterials for imaging through skull with imperfections. *Front. Mech. Eng.* **6**, 55.
[38] Tian Z H, Shen C, Li J, Reit E, Gu Y, Fu H, Cummer S A and Huang T J. 2019. Programmable acoustic metasurfaces. *Adv. Funct. Mater.* **29**, 1808489.
[39] Zhao S-D, Chen A-L, Wang Y-S and Zhang C. 2018. Continuously tunable acoustic metasurface for transmitted wavefront modulation. *Phys. Rev. Appl.* **10**, 054066.
[40] Cao W K, Zhang C, Wu L T, Guo K Q, Ke J C, Cui T J and Cheng Q. 2021. Tunable acoustic metasurface for three-dimensional wave manipulations. *Phys. Rev. Appl.* **15**, 024026.
[41] Kinsler L E et al. 2000. *Fundamentals of Acoustics* 4th edn. (John Wiley, New York)
[42] Fink M. 1992. Time reversal of ultrasonic fields. I. Basic principles. *IEEE Trans. Ultrason. Ferroelectr. Freq. Control* **39**, 555–566.
[43] Fink M and Prada C. 2001. Acoustic time-reversal mirrors. *Inverse Probl.* **17**, R1–R38.
[44] Fu Y F, Kabir I I, Yeoh G H and Peng Z. 2021. A review on polymer-based materials for underwater sound absorption. *Polym. Test.* **96**, 107115.
[45] Waterman P C and Truell R. 1961. Multiple scattering of waves. *J. Math. Phys.* **2**, 512–537.
[46] Xiao J X, Zhan B, He M, Qi X, Zhang Y, Guo H, Qu Y, Zhong W and Gu J. 2025. Mechanically robust and thermal insulating nanofiber elastomer for hydrophobic, corrosion-resistant, and flexible multifunctional electromagnetic wave absorbers. *Adv. Funct. Mater.* **35**, 2419266.
[47] Nuncio Zuniga A and Fink W. 2023. Suitability of silicone in soft-robotic exploration of terrestrial and extraterrestrial ocean worlds. *Space Sci. Technol.* **29**, 47–56.
[48] Xavier J R. 2022. Superior surface protection, mechanical and hydrophobic properties of silanized tungsten carbide nanoparticles encapsulated epoxy nanocomposite coated steel structures in marine environment. *Silicon* **14**, 11147–11161.
[49] Shivapooja P, Cao C, Orihuela B, Levering V, Zhao X, Rittschof D and López G P. 2016. Incorporation of silicone oil into elastomers enhances barnacle detachment by active surface strain. *Biofouling* **32**, 1017–1028.
[50] Kolle S et al. 2022. On the mechanism of marine fouling-prevention performance of oil-containing silicone elastomers. *Sci. Rep.* **12**, 11799.
[51] Sun J W, Xiong W, Zhang L, Guo X, Song Y and Wu L. 2025. Continuous multi-material additive manufacturing. *Research* **8**, 0889.
[52] Bandyopadhyay A and Heer B. 2018. Additive manufacturing of multi-material structures. *Mater. Sci. Eng.* **129**, 1–16.
[53] Wang Y L and Willenbacher N. 2022. Phase-change-enabled, rapid, high-resolution direct ink writing of soft silicone. *Adv. Mater.* **34**, 2109240.
[54] Shang E W, Li G, Zhao Z, Zhang N, Fan D and Liu Y. 2023. Laser-assisted direct ink writing for high-fidelity fabrication of elastomeric complex structures. *Adv. Mater. Interfaces* **10**, 2300300.
[55] Cochard E, Prada C, Aubry J F and Fink M. 2009. Ultrasonic focusing through the ribs using the DORT method. *Med. Phys.* **36**, 3495–3503.
[56] Liu H-L, Hsu C-L, Huang S-M and Hsi Y-W. 2010. Focal beam distortion and treatment planning for transrib focused ultrasound thermal therapy: a feasibility study using a two-dimensional ultrasound phased array. *Med. Phys.* **37**, 848–860.
[57] Chen J et al. 2025. Achieving high-performance transcranial ultrasound transmission through Mie and Fano resonance in flexible metamaterials. *Adv. Sci.* **12**, 2500170.
[58] Hu Z T, Yang Y, Xu L, Hao Y and Chen H. 2022. Binary acoustic metasurfaces for dynamic focusing of transcranial ultrasound. *Front. Neurosci.* **16**, 984953.
[59] Daniel M, Attali D, Tiennot T, Tanter M and Aubry J F. 2024. Multifrequency transcranial ultrasound holography with acoustic lenses. *Phys. Rev. Appl.* **21**, 014011.
[60] Chen Q P, Xie Y, Cao H, He Z, Wang D and Guo S. 2022. Ultrasonic inspection of curved structures with a hemispherical-omnidirectional ultrasonic probe via linear scan SAFT imaging. *NDT&E* **129**, 102650.
[61] Lyu D, Li X, Zhang R and Zhang S. 2022. Ultrasonic measurement model-based non-destructive detection method for curved components using an immersion spherically focused transducer. *Nondestr. Test. Eval.* **37**, 184–202.
[62] Revel G M, Pandarese G and Cavuto A. 2013. Advanced ultrasonic non-destructive testing for damage detection on thick and curved composite elements for constructions. *J. Sandw. Struct. Mater.* **15**, 5–24.
[63] Zhang H K, Wang Q, Fink M and Ma G. 2024. Optimizing multi-user indoor sound communications with acoustic reconfigurable metasurfaces. *Nat. Commun.* **15**, 1270.
[64] Ma G C, Fan X, Sheng P and Fink M. 2018. Shaping reverberating sound fields with an actively tunable metasurface. *Proc. Natl Acad. Sci. USA* **115**, 6638–6643.
[65] Lin Q, Wang J, Cai F, Zhang R, Zhao D, Xia X, Wang J and Zheng H. 2021. A deep learning approach for the fast generation of acoustic holograms. *J. Acoust. Soc. Am.* **149**, 2312–2322.
[66] Miao X-B, Dong H-W, Zhao S-D, Fan S-W, Huang G, Shen C and Wang Y-S. 2023. Deep-learning-aided metasurface design for megapixel acoustic hologram. *Appl. Phys. Rev.* **10**, 021411.

[67] Lee M H, Lew H M, Youn S, Kim T and Hwang J Y. 2022. Deep learning-based framework for fast and accurate acoustic hologram generation. *IEEE Trans. Ultrason. Ferroelectr. Freq. Control* **69**, 3353–3366.

[68] Dong H-W et al. 2024. Inverse design of phononic metastructured materials. *Mater. Today Chem.* **80**, 824–855.

[69] Zhang J H, Zhou N, Dong E, Zhang C, Song Z, Liu S, Yang C, Su X, Wang S and Zhang Y. 2024. Soft bio-metamaterials with high acoustic transparency and gradient refractive index for tunable acoustic beamformer. *Matter* **7**, 3857–3875.

[70] Yu K H, Fang N X, Huang G and Wang Q. 2018. Magnetoactive acoustic metamaterials. *Adv. Mater.* **30**, 1706348.

[71] Lee K H, Yu K, Al Ba'ba'a H, Xin A, Feng Z and Wang Q. 2020. Sharkskin-inspired magnetoactive reconfigurable acoustic metamaterials. *Research* **2020**, 4825185.

[72] Zhang J H, Zhang T, Dong E, Zhang C, Lin Z, Song Z, Li H, Fang N X and Zhang Y. 2022. Bioinspired hydrogel jellyfish with mechanical flexibility and acoustic transparency. *Cell Rep. Phys. Sci.* **3**, 101081.